How to cite: *Angew. Chem. Int. Ed.* **2023,** *62,* e202215552
International Edition: doi.org/10.1002/anie.202215552
German Edition: doi.org/10.1002/ange.202215552

Aqueous Zn Metal Batteries

Comprehensive H_2O Molecules Regulation via Deep Eutectic Solvents for Ultra-Stable Zinc Metal Anode

Ming Li, Xuanpeng Wang, Jisong Hu, Jiexin Zhu, Chaojiang Niu, Huazhang Zhang, Cong Li, Buke Wu, Chunhua Han,* and Liqiang Mai**

Abstract: The corrosion, parasitic reactions, and aggravated dendrite growth severely restrict development of aqueous Zn metal batteries. Here, we report a novel strategy to break the hydrogen bond network between water molecules and construct the $Zn(TFSI)_2$-sulfolane-H_2O deep eutectic solvents. This strategy cuts off the transfer of protons/hydroxides and inhibits the activity of H_2O, as reflected in a much lower freezing point ($<-80\,°C$), a significantly larger electrochemical stable window (>3 V), and suppressed evaporative water from electrolytes. Stable Zn plating/stripping for over 9600 h was obtained. Based on experimental characterizations and theoretical simulations, it has been proved that sulfolane can effectively regulate solvation shell and simultaneously build the multifunctional Zn-electrolyte interface. Moreover, the multi-layer homemade modular cell and 1.32 Ah pouch cell further confirm its prospect for practical application.

[*] M. Li, J. Zhu, C. Li, Prof. C. Han, Prof. L. Mai
State Key Laboratory of Advanced Technology for Materials Synthesis and Processing, Wuhan University of Technology
Hubei, Wuhan 430070 (China)
E-mail: hch5927@whut.edu.cn
mlq518@whut.edu.cn

Dr. X. Wang, Dr. H. Zhang
Department of Physical Science & Technology,
School of Science, Wuhan University of Technology
Wuhan 430070 (China)
E-mail: wxp122525691@whut.edu.cn

Dr. X. Wang, Prof. L. Mai
Hubei Longzhong Laboratory
Xiangyang, Hubei, 441000 (China)

J. Hu
School of Optical and Electronic Information,
Huazhong University of Science and Technology
Wuhan 430074 (China)

Prof. C. Niu
School of Materials Science and Engineering,
Zhengzhou University
Zhengzhou 450001 (China)

B. Wu
Department of Mechanical and Energy Engineering,
Southern University of Science and Technology
Shenzhen 518055 (China)

Introduction

Aqueous Zn metal batteries (ZMBs) are receiving tremendous attention due to their low cost, intrinsic safety, and high theoretical capacity of metallic Zn electrode ($820\,mA\,hg^{-1}/5854\,mAh\,cm^{-3}$).[1] Unfortunately, limited by the lower standard electrode potential of Zn^{2+}/Zn (-0.762 V versus (vs) standard hydrogen electrode), Zn metal is thermodynamically unstable in the water environment during the electroplating and stripping process, resulting in severe parasitic reactions, corrosion/passivation, and dendrites growth of the Zn anode.[2] The reasons for the above process can be summarized as follows. On the one hand, owing to the coordination structure of Zn^{2+} ions in mild-neutral aqueous electrolytes, a large amount of free water combined with Zn^{2+} ions (0.74 Å) to form large-sized hydrated $Zn(H_2O)_n^{2+}$ ions with a highly oriented and ordered structure.[3] The solvated $Zn(H_2O)_n^{2+}$ located in the electric double layer must therefore overcome the energy barrier to de-solvate and release a large number of electrochemically reactive free water molecules to complete the Zn plating process: $Zn(H_2O)_n^{2+} \leftrightarrow Zn^{2+} + n\,H_2O$.[4] This kind of active isolated water molecules holds weakened H–O bonds, thus leading to the deprotonation of water and promotion of water hydrolysis. It causes easier decomposition of active water molecules in the vicinity of the Zn foil to produce hydrogen, especially at the high redox overpotential, which in turn causes an increased pH of the local microenvironment near metallic Zn ($2\,H_2O + 2\,e^- \leftrightarrow 2\,OH^- + H_2$).[5] It further connives the formation of side reaction products, which are usually basic zinc salts/oxides $(Zn_x(OH)_y(Anion)_z^{+2/+1}/ZnO/Zn(OH)_2)$.[6] As the Zn electrode is corroded and passivated, the uneven deposition is exacerbated and combined with uncontrolled two-dimensional (2D) diffusion of Zn^{2+} ions on the Zn metal surface, ultimately leading to the severe growth of Zn dendrites.[7] Hence, how to effectively inhibit the participation of water molecules in the solvated structure and hinder the 2D diffusion of Zn^{2+} ions is one of the keys to improving the stability of Zn anodes.[8]

For another aspect, the effect of abundant H_2O–H_2O hydrogen bonds (H–O···H) in pure aqueous electrolytes on metallic Zn anode cannot be ignored.[9] In fact, the long-range organized H_2O–H_2O hydrogen bond network can significantly affect the hydrogen evolution reaction (HER) process, reflected in the ultra-fast diffusion of the proton and hydroxide ions through the Grotthuss mechanism,[10] and the separation of ionic products in the Volmer step.[11] It

ultimately accelerates the decomposition of H_2O and related parasitic reactions on the Zn surface. Therefore, breaking the hydrogen bond network between H_2O molecules to inhibit the water activity and suppress HER in the aqueous electrolytes is one of the efficacious ways to improve the stability of the Zn anode fundamentally.[12] Moreover, the existence of hydrogen bonds can significantly affect the physical and chemical properties of electrolytes, including freezing point, viscosity, and solubility.[13] At low temperatures ($<0\,°C$), hydrogen bonds can change water from liquid to solid, which seriously affects the regular operation of the battery and limits the range of service environment under different conditions.

Here, for the first time, we propose a new versatile strategy to configure $Zn(TFSI)_2$-sulfolane-water hybrid electrolytes for improving the stability of Zn anodes, which simultaneously achieves hydrogen bond reconfiguration, solvation shell optimization, and multifunctional Zn-electrolyte interface through a comprehensive manipulation of H_2O molecules. Unlike other sulfone-based additives, the introduction of ultra-high concentrations of sulfolane (87 wt % or 93 %) exhibits deep eutectic solvents (DES) system properties and eliminates the vast majority bulk free water.[14] This electrolyte strategy with excellent environmental adaptability is easier and cheaper to prepare than general DES electrolytes, and high concentration "water-in-salt" electrolytes.[15] In fact, the properties of electrolyte we prepared is between the pure organic electrolytes and the aqueous electrolytes. Importantly, as an affordable, environmentally friendly, and aprotic polar solvent, sulfolane can provide more hydrogen bond acceptors than water molecules due to its unique atomic configuration, which facilitates the breaking of the intrinsic H_2O–H_2O hydrogen bonds (H–O–H···O–H) and participating in the formation of new hydrogen bond network (sulfolane-water: S=O···H–O). It inhibits the proton auto-transport reaction related to HER mentioned above. As a result, the ultra-low freezing point ($<-80\,°C$), wide electrochemical stable window (>3 V), and inhibited evaporation under the atmosphere are achieved due to the inhibited water activity. Experiments and theoretical simulations confirm and reveal the in-depth mechanism for the excellent suppression of parasitic reactions and dendrite growth. Benefitting from efficient electrolyte optimization, the ultra-long cycle life of over 9600 h in fabricated Zn symmetric batteries and the splendid Coulombic efficiency (CE) of 99.3 % in Zn||Ti batteries are achieved, which proves the ultra-stable plating/stripping of Zn^{2+}. As a proof of concept, the fabricated ZMBs with $V_2O_5{\cdot}nH_2O$ cathode exhibit significantly improved cycle performance (84 % after 2000 cycles), CE, and self-discharge suppression (96 % after 48 h), and stable low-temperature operation even at $-20\,°C$. In particular, the high-capacity (1.32 Ah) pouch cell with high performance were also assembled to provide a referable model for practicable applications. This comprehensive understanding provides new insights and avenues to develop stable practical electrolytes for ZMBs and even other aqueous metal batteries.

Results and Discussion

As shown in Figure S1, the traditional hydrogen bond consists of two parts: a proton donor with a hydrogen atom and a proton acceptor with at least one lone pair of electrons. The proton acceptor is usually an atom with large electronegativity and small radius (O, N, S, etc.). Theoretically, sulfolane can form two hydrogen bonds with the water molecule due to the presence of two lone pairs of electrons. Density functional theory (DFT) calculations indicate the different hydrogen bond lengths of S=O···H–O (1.918 Å) and H–O···H–O (1.964 Å). The slightly shorter bond length of sulfolane-water implies a stronger hydrogen bond than H_2O–H_2O (Figure 1a and b). The higher binding energies of -0.471 eV ($10.86\,kcal\,mol^{-1}$) than -0.222 eV ($5.12\,kcal\,mol^{-1}$) demonstrate the stronger hydrogen bond between sulfolane and water molecule. Further, electrostatic potential calculations demonstrate that S=O is more attractive for hydrogen atoms due to a more negative charge distribution than O–H, which is consistent with enhanced hydrogen bond strength (Figure 1c).

In order to further explore the influence of sulfolane on hydrogen bonds and the activity of H_2O, a series of characterizations were carried out. The in situ attenuated total reflection-Fourier transform infrared ray (ATR-FTIR) indicates three distinct changes (Figure 1d; Figure S2). The strong peaks at 3200–3700 cm^{-1} and 1550–1750 cm^{-1} correspond to O–H stretching and bending vibration modes of H_2O molecules, respectively.[16] The two vibrational bonds appearing in the range 1040–1390 cm^{-1} with significantly increasing strength correspond to symmetric S=O stretching (1140 cm^{-1}) and asymmetric S=O stretching (1290 cm^{-1}) from sulfolane, respectively (Figure S3).[17] For the O–H stretching model, the different wavenumber of 3280, 3470, and 3590 cm^{-1} reflects H_2O molecules environments with different configurations.[18] The lower frequency of O–H stretching vibration indicates the weakened bond energy of O–H in H_2O, meaning that abundant hydrogen bonds are formed in H_2O.[19] The hydrogen bonds associate with each other to form larger bulk molecules, which reduces the system's energy, resulting in a reduction in the vibrational frequency of the H–O bond and high wavenumber. Hence, according to the wavenumber of the peak, the 3280, 3470, and 3590 cm^{-1} can be classified as three types of H_2O molecule environments: bulk H_2O, cluster sulfolane-H_2O and isolated sulfolane-H_2O.[1b,11b,20] In pure water, the corresponding peak locates at 3240 cm^{-1} suggesting a large number of bulk H_2O with tetrahedral H_2O–H_2O (H–O···H) hydrogen bond network. With the addition of sulfolane, the wavenumber of the O–H stretching vibration gradually increases while the intensity gradually decreases and broadens. A higher wavenumber indicates a higher bond energy of O–H in H_2O due to the decrease in the number of hydrogen bonds and the disruption of the hydrogen bond network.[21] In addition to peak shift, both the O–H stretching and bending vibration of intensity decrease dramatically due to decreased water content. Further, 1 M $Zn(TFSI)_2/ZnSO_4$ electrolytes based on pure water or hybrid solvents were conducted by ex situ FTIR. For the

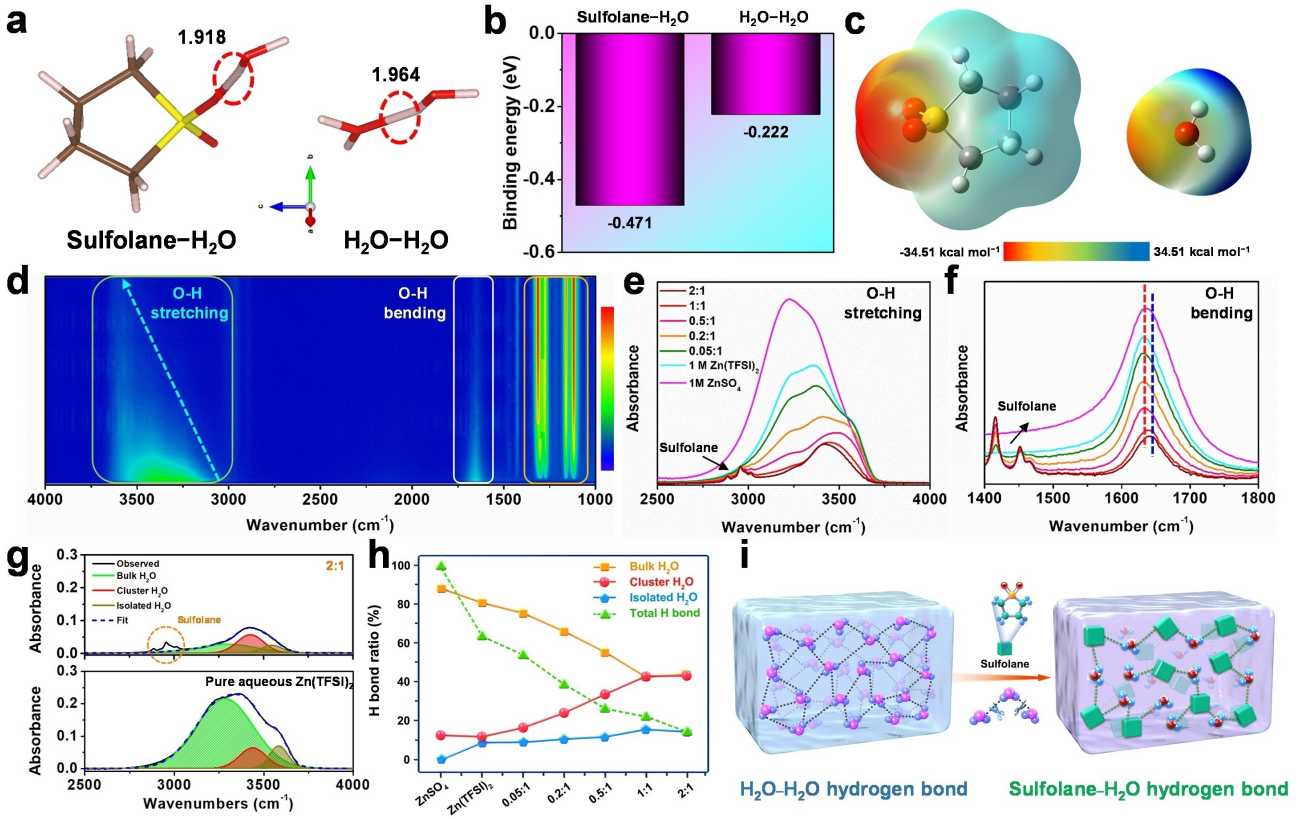

Figure 1. a) DFT calculation of hydrogen bond length and b) corresponding binding energy. c) Electrostatic potential maps of sulfolane and H_2O molecule. d) In situ ATR-FTIR spectra of water with the introduction of sulfolane. e), f) FTIR spectra of pure aqueous 1 M $ZnSO_4$ electrolyte, pure aqueous 1 M $Zn(TFSI)_2$ electrolytes, and 1 M $Zn(TFSI)_2$ sulfolane-H_2O hybrid electrolytes with different molar ratios (0.05 : 1, 0.2 : 1, 0.5 : 1, 1 : 1, 2 : 1) g) The fitted FTIR spectra of pure aqueous $Zn(TFSI)_2$ electrolyte and hybrid electrolyte (2 : 1). h) The proportions and total of bulk H_2O, cluster H_2O, and isolated H_2O in the different electrolytes. i) Schematic diagram of the hydrogen bond reconstruction involving sulfolane.

O–H stretching and bending model, the spectra exhibited similar changes, i.e. a slight increase in wavenumber and a decrease in intensity due to the addition of sulfolane (Figure 1e and f). In particular, the higher intensity of H_2O peaks (O–H stretching and bending) appears in pure aqueous $ZnSO_4$ than $Zn(TFSI)_2$ electrolyte due to the more crowded molecules of $TFSI^-$ and reduced bulk H_2O. The fitted FTIR spectra were used to better reveal the ratio of the three types of H_2O configuration calculated from the fitted peak area (Figure 1g; Figure S4). A significant decrease of 85.46 % in the total number of H_2O can be observed. Correspondingly, the proportions of cluster and isolated H_2O rise to 42.58 % and 13.78 %, respectively (Figure 1h). The in situ/ex situ FTIR results strongly demonstrate that the addition of sulfolane breaks the bulk H_2O–H_2O hydrogen bond network and forms a new type of hydrogen bond of sulfolane-H_2O (Figure 1i).

Molecular dynamics (MD) simulations were conducted to reveal the 1 M $Zn(TFSI)_2$ electrolyte structure in pure water and sulfolane hybrid solvents (Figure S5). As shown in Figure 2a, the numerous bulk water of $(H_2O)_n$ surround solvated Zn^{2+} ions in pure aqueous electrolyte. To precisely analyze the local structures in the electrolytes, the radial distribution function (RDF), g(r), and N(r) were applied to further reveal the Zn^{2+} solvation shell and the Zn^{2+}–H_2O interactions. In Figure 2a, the RDF between Zn^{2+} and the O atom of water molecules (O_W) shows a coordination peak at 1.67 Å with a coordination number of 4.07, which indicates the presence of about four H_2O molecules in the solvated structure of the Zn^{2+} ion. In hybrid electrolyte, the H_2O molecules are in a dispersed state, and bulk water of $(H_2O)_n$ is significantly suppressed in Figure 2b. The RDF between Zn^{2+} and the O atom of H_2O molecules shows a coordination peak at 1.68 Å with a coordination number of 1.77, implying less than two H_2O molecules in the solvated structure. In comparison, the RDF between Zn^{2+} and the S atom of sulfolane shows a coordination peak at 3.17 Å with a coordination number of 2.67, demonstrating that the sulfolane can participate in solvation shell and replace water molecules. MD results further prove that the addition of sulfolane not only significantly broke bulk H_2O molecules, but also affected the solvation shell of Zn^{2+} ions. The dramatically reduced H_2O molecules in the solvation shell are beneficial to inhibiting the corrosion of the Zn anode surface caused by the active H_2O molecules generated in the desolvation process.[14c] The change in the number of hydrogen bonds calculated by MD simulations further indicate that sulfolane can ligate with H_2O molecules to form hydrogen bonds while breaking the H_2O–H_2O hydrogen

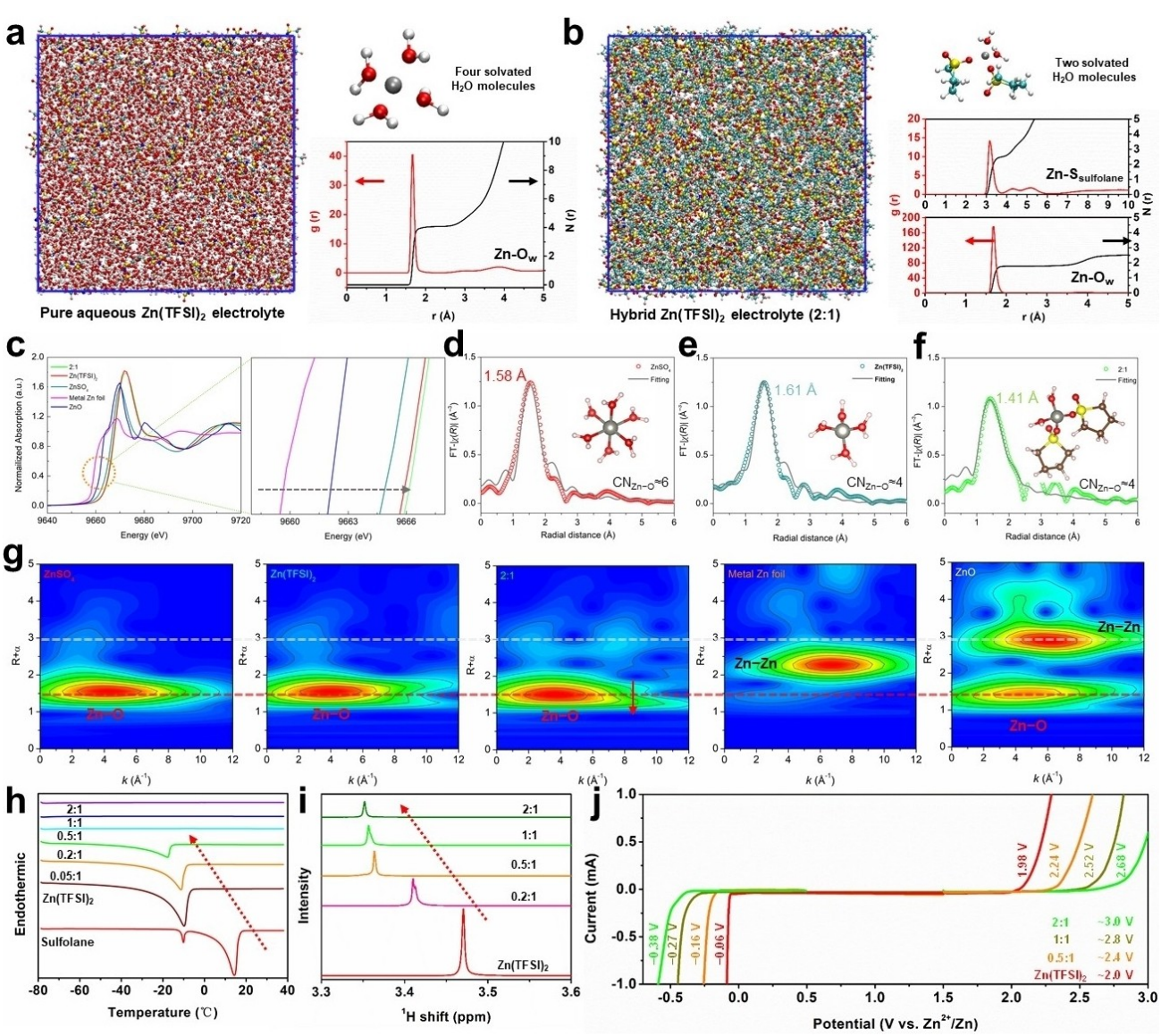

Figure 2. a) Snapshot of pure aqueous 1 M $Zn(TFSI)_2$ electrolyte and th e corresponding RDF g(r) and coordination number N(r) of Zn–O_W in MD simulation. b) Snapshot of sulfolane-H_2O $Zn(TFSI)_2$ hybrid electrolyte (2:1) and the corresponding RDF g(r) and coordination number N(r) of Zn–O_W/Zn–$S_{sulfolane}$ in MD simulation. c) The normalized Zn K-edge XANES spectra and enlarged Zn K-edge XANES spectra of ZnO, metal Zn, $ZnSO_4$, $Zn(TFSI)_2$, and 2:1. The FT-EXAFS fitting spectra at R space for d) $ZnSO_4$, e) $Zn(TFSI)_2$ and f) 2:1. g) Wavelet transforms of Zn K-edge XANES signals for $ZnSO_4$, $Zn(TFSI)_2$, and 2:1, metal Zn, and ZnO. h) DSC results, i) ^1H NMR spectra, and j) Electrochemical stability windows for pure aqueous $Zn(TFSI)_2$ electrolyte and sulfolane-H_2O hybrid electrolytes determined by LSV tests.

bond, which is consistent with pervious FTIR results (Figure S6).

The X-ray adsorption fine structure (XAFS) technique was used to further elucidate the local atomic arrangement around Zn^{2+} ions, especially the first-layer coordination states. Figure 2c show the Zn K-edge X-ray adsorption near-edge structure (XANES) spectra of 2:1 electrolyte, $Zn(TFSI)_2$ electrolyte, $ZnSO_4$ electrolyte, ZnO, metal Zn foil for comparison. Interestingly, the near-edge absorbed energy is sorted according to Zn < ZnO < $ZnSO_4$ electrolyte < $Zn(TFSI)_2$ electrolyte < 2:1 electrolyte. The higher-energy region indicates that the solvated Zn^{2+} ions with unique local structure present a higher valence in the electrolytes compared to metal Zn^0 foil and $Zn^{(2+)}O$, which means that the decreased average electron density around Zn^{2+}.[22] Interestingly, the 2:1 electrolyte exhibites the highest near-side adsorption energy among three different electrolytes indicating the lowest electron density after the introduction of sulfolane. It demonstrates that sulfolane enters the solvation sheath and alters the electron distribution of solvated Zn^{2+} ions. More structural information are revealed based on Fourier-transformed extended X-ray adsorption fine structure (FT-EXAFS) and a higher atomic number of scattering atom in coordination shell normally leads to a higher k shift (Figure S7).[23] The 2:1 hybrid electrolyte demonstrates significantly shorter Zn–O bond

radial distances (1.41 Å) of compared to pure aqueous ZnSO4 (1.58 Å) and $Zn(TFSI)_2$ (1.61 Å), in accordance with the results of MD simulations, indicating an enhanced interaction between Zn^{2+} and solvents. The FT-EXAFS spectra of different electrolytes are fitted to precisely obtain the local structures. The corresponding coordination numbers (CN) of Zn–O in ZnSO4 ($\approx$6), $Zn(TFSI)_2$ ($\approx$4), and 2:1 ($\approx$4) electrolytes highly consistent with the MD results (Figure 2d–f). Moreover, the wavelet transformed (WT) EXAFS was utilized to analyze Zn–O coordination (Figure 2g). The similar CN, WT maximum values, transfer trends indicate that it is still the Zn–O coordination after the introduction of sulfolane in electrolytes. Therefore, combined with theoretical calculation and experimental characterization, we strongly confirmed the regulation of sulfolane on solvation structure of Zn^{2+} and thereby reduced the active free water molecules produced by desolvation on the Zn surface.

A series of related characterizations are used to investigate the properties of different electrolytes. Differential scanning calorimetry (DSC) curves show the typical endothermic peak associated with the glass-transition temperature (freeze-point) in the aqueous electrolyte (Figure 2h). Obviously, the transition temperature decreases significantly and even below −80 °C as the proportion of sulfolane added rises compared to pure aqueous electrolytes.[24] The H_2O–H_2O hydrogen bond network formed by a large number of bulk water molecules brings a higher freezing point (0 °C). The pristine pure sulfolane has a high freezing point of >14 °C. Interestingly, $Zn(TFSI)_2$-sulfolane-H_2O hybrid electrolytes exhibit obvious DES property and achieving a lower freeze-point <−80 °C. The effect of sulfolane-H_2O hydrogen bond is further supported by the observation of ^1H nuclear magnetic resonance (NMR) spectra (Figure 2i). The pure aqueous $Zn(TFSI)_2$ electrolyte shows a higher field. It reflects a stronger density of electron clouds in the periphery of hydrogen nuclei, which is influenced by the electronegativity of the functional group linked to hydrogen.[25] The apparent downshifts with larger σ values appeared and were proportional to the addition of sulfolane, suggesting a reduced electron cloud density.[26] This can be attributed to the de-shielding effect resulting from the stronger electronegativity of the S=O group, which is consistent with previous theoretical calculations. Although high concentrations of sulfolane also lead to a moderate increase in viscosity, it is still lower than that most of the ionic liquids, highly concentrated "water-in-salt" electrolytes, eutectic electrolytes, and quasi-solid state electrolytes due to higher water content (Figure S8a).[27] The electrochemical stability windows (ESW) of electrolytes were evaluated by electrochemical linear sweep voltammetry (LSV) based on the 2025-coin battery (SS mesh as work electrode, Zn foil as a counter electrode and reference electrode) at a scan rate of 0.2 mV s^{-1} (Figure 2j). The widened ESW from 2.0 to 3.0 V can be achieved owing to suppression of water splitting in hybrid electrolytes. In contrast, the hydrogen bond network formed by water molecules promotes the transfer of protons/hydroxides and the separation of ionic products in the Volmer step, which promotes the HER.[28] The addition of aprotic polar solvent sulfolane breaks the intrinsic bulk H_2O–H_2O hydrogen bond network while forming cluster sulfolane-H_2O hydrogen bond. It impedes the diffusion and separation of the proton/hydroxide/ion products and therefore inhibits the water activity. In addition, the higher bond energy of O–H in H_2O due to sulfolane-H_2O bond (FTIR blue shift) intensifies the difficulty of water splitting. The mild pH values significantly prove the great effect of sulfolane in inhibiting water activity and cutting off the H_2O–H_2O hydrogen bond (Figure S8b). Additionally, the instability of water molecules is also reflected in the evaporative properties (Figure S9).

Since the growth of Zn dendrites occurs mainly at the interface between the Zn anode and the electrolyte, there is also necessary to investigate the interaction behavior of Zn crystals with H_2O and sulfolane molecules at the electrode/electrolyte interface.[29] Here, considering the unique hexagonal close-packed (hcp) structure of Zn, adsorption energy and charge density difference of H_2O and sulfolane molecule on Zn (0001) and (1000) surface were firstly implemented by DFT calculations (Figure S10 and S11a,b). The calculations show that the (0001) plane has a lower surface energy, which means that this plane is more easily exposed to the electrolyte than (1000) planes (Figure S11c). As show in Figure 3a and S11d–f, both crystal planes show the lower adsorption energy calculated for sulfolane (−0.44/−0.84 eV) than H_2O (−0.27/−0.28 eV). In addition, the wetting angle of sulfolane on the Zn foil surface is significantly less than that of water, suggesting better zincophilicity (Figure S12). The larger overlapping area of electron cloud between O atom and Zn (0001) surface indicate that sulfolane molecules can be preferentially adsorbed on the Zn surface, especially in sulfolane-rich environments (87 or 93 wt %) (Figure 3a). Hence, these results further strongly prove that the stable interface constructed by sulfolane adsorption layer in hybrid electrolytes replace the active Zn–H_2O interface in pure aqueous electrolytes.

The absorbed sulfolane layer serves to insulate the active water molecules while preventing HER occurring on the surface of the Zn foil. The electric field distribution is also one of the essential factors leading to the growth of dendrites.[30] Therefore, a multiphysics model based on a finite element analysis (FEA) is applied by COMSOL multiphysics to investigate the distribution of the electric field in two cases with or without sulfolane adsorption. As shown in Figure 3b, the electric field is uneven and concentrated on the top of the crystal Zn seeds in pure aqueous $Zn(TFSI)_2$ electrolyte due to the tip charge accumulation effect. On the contrary, the electric field at the tip is significantly suppressed in hybrid electrolyte and is more evenly distributed in the non-tip area. This indicates that the sulfolane adsorption layer can avoid the tip effect in the electroplating process and suppress the growth of Zn dendrites. In addition to the impact of electric field, the two-dimensional (2D) diffusion of Zn^{2+} ions on the metallic Zn surface should not be neglected as well. According to classical electrochemical theory, the desolvated Zn^{2+} within the electric double layer (EDL) will be absorbed into the Zn

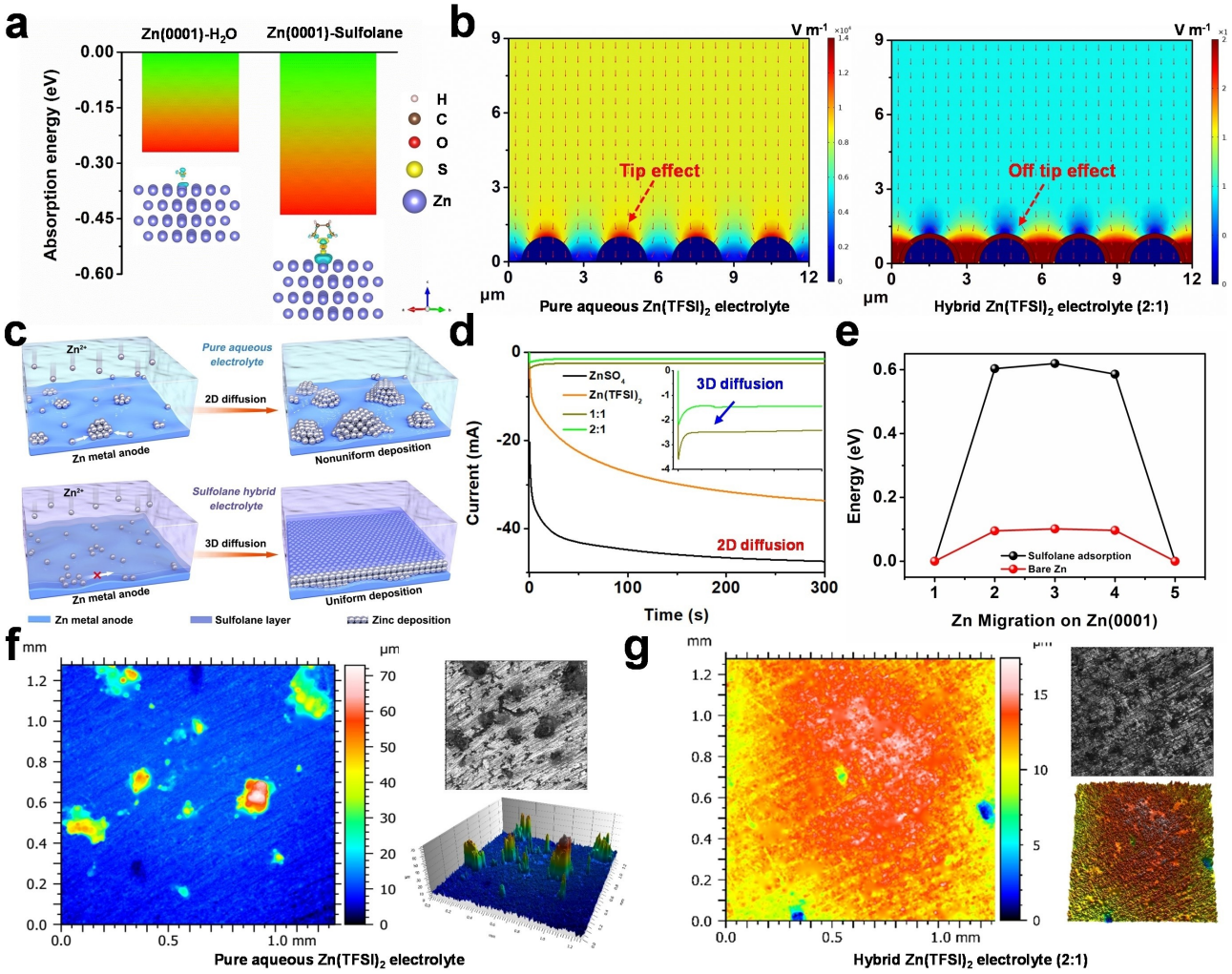

Figure 3. a) Adsorption energy and charge density difference comparison of H_2O and sulfolane molecule on Zn (0001) crystal plane. The charge density difference of the isovalue chosen to plot the isosurface is 0.0005 e/Å^{-3}. The cyan and yellow areas indicate electron depletion and accumulation, respectively. b) The electrical field models by FEA in the pure aqueous 1 M $Zn(TFSI)_2$ electrolyte and sulfolane-H_2O hybrid electrolyte, respectively. c) Schematically diagrams of sulfolane adsorption and subsequent Zn electroplating and diffusion processes. d) Chronoamperograms of Zn foils in different electrolytes under −0.15 V within 300 s. e) Zn migration energy on Zn (0001): Zn with sulfolane and bare Zn. The 3D confocal microscope images for the surface of the Zn in (f) pure aqueous 1 M $Zn(TFSI)_2$ electrolyte and g) sulfolane-H_2O hybrid electrolyte (2:1).

surface and await electron reaction.[7,8d] However, the most convenient approach is to aggregate on the Zn nuclei and then form larger Zn nuclei, thus minimizing the surface energy (Figure 3c). This leads to uncontrollable 2D diffusion of Zn^{2+} ions on the Zn surface and exacerbates the formation of Zn dendrites. Chronoamperometry (CA) was further carried out to examine the diffusion type of Zn^{2+} for symmetric Zn coin batteries. When the Zn electrode with pure aqueous electrolytes were applied with a voltage of −150 mV, the current held increased for 300 seconds, indicating a constant 2D diffusion process (Figure 3d). The high current implies a non-uniform Zn deposition as well as a significant increase in specific surface area.[31] On the contrary, the hybrid electrolyte exhibits a severely constrained 2D diffusion and stable 3D diffusion from the beginning due to the hindrance of sulfolane on the Zn surface. In particular, the current of 1:1 and 2:1 are decreased during Zn plating. It can be attributed to the self-smoothing process, which fill the surface gullies formed by sandpaper grinding resulting in a reduction of the specific surface area in initial state (Figure 3c; Figure S13).

Further, Zn migration energy calculations indicate that the 2D diffusion barriers of Zn^{2+} ions increase significantly on the sulfolane-Zn interface (0.62 eV) than bare Zn (0.1 eV), which is consistent with previous results (Figure 3e and S14). The 3D height images of Zn symmetric batteries with different electrolytes directly prove the suppression of Zn dendrites (Figure 3f and g). In pure aqueous electrolyte, Zn surface show significant dendrite growth after 30 cycles (1 mA cm^{-2}, 1 mAh cm^{-2}) compared to the original Zn foil (Figure S15). As a comparison, a dendrite-free Zn electroplating can be realized in sulfolane-H_2O hybrid electrolyte.

Through previous experimental characterization and theoretical analysis, the excellent effects of sulfolane-H_2O

hybrid electrolyte in reorganizing hydrogen bonds to anchor active free water, optimizing solvation shell, and inhibiting the growth of Zn dendrites have been in-depth demonstrated. Subsequently, reversible Zn plating and stripping measurements were further performed to investigate the electrochemical performance in practical applications. As shown in Figure 4a, the Zn||Zn symmetric coin using hybrid electrolyte can stably cycle over 8800 h at 0.5 mA cm^{-2}/0.5 mAh cm^{-2} and over 9600 h at 1 mA cm^{-2}/1 mAh cm^{-2} without significantly increased polarization or "soft short".[32] To our knowledge, this is the best performance reported to date (Table S1). On the other hand, those using pure aqueous electrolyte or with a fewer content of sulfolane are short-circuited less than 200 h of cycling under the same conditions (Figure S16). SEM images show a completely different Zn plating morphology (Figure S17). Homogeneous and dense plating in hybrid electrolyte replaces mossy-like plating of clusters in pure aqueous electrolytes. XRD results indicate that parasitic reactions accompanying inhomogeneous plating process inevitably occur and produce ZnO and $Zn_x(OH)_y(Anion)_z^{+2/+1}$ in pure electrolyte. At the same time, almost no signals of by-products are visible in the hybrid electrolyte (Figure S18). Even under harsher conditions, including high current density/high capacity (5 mA/5 mAh cm^{-2}), ultra-high Zn utilization (>60 %), and low temperature of −20 °C, stable cycling performances far exceeds that of pure aqueous electrolytes can be achieved (Figure S19–S21). Further, the immersion test of the Zn foil in the electrolyte proved the same excellent corrosion protection effect in the non-working state (Figure S22 and S23).

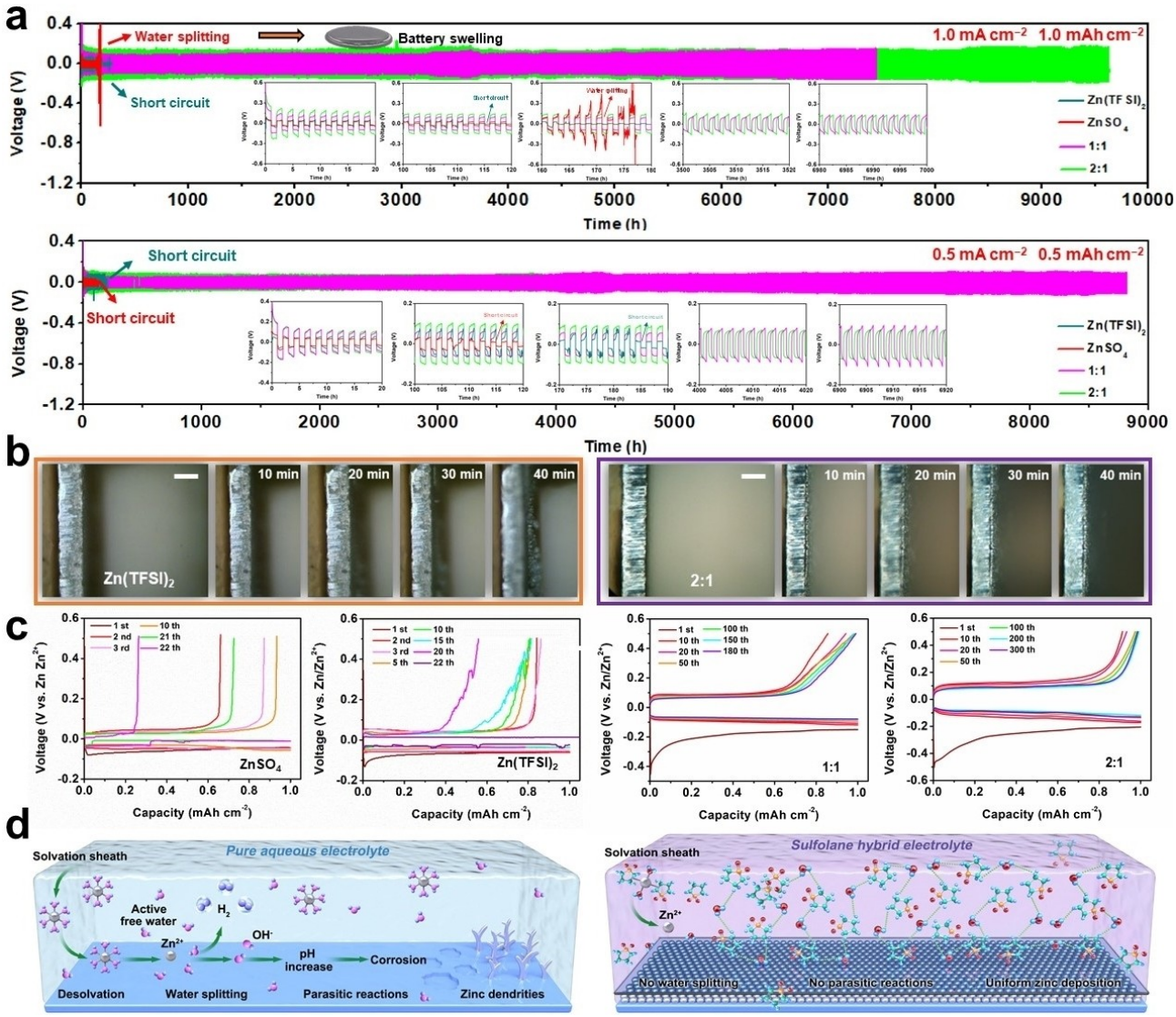

Figure 4. a) Galvanostatic cycling of symmetrical coin batteries in different electrolytes of $ZnSO_4$, $Zn(TFSI)_2$, 1:1, and 2:1. b) Cross-sectional Zn deposition morphology with different electrolytes in a symmetrical Zn battery at a current density of 5 mA cm^{-2} using an in situ optical microscope. c) Voltage profiles of Zn||Ti batteries under different electrolyte system. d) Schemes illustrating different reaction processes of Zn^{2+} solvation shell and corresponding interfacial interaction between pure aqueous electrolyte and sulfolane-H_2O hybrid electrolyte.

In situ optical microscopic observation provides an intuitive view of Zn plating in different electrolytes (Figure 4b; Figure S24). In pure aqueous electrolyte, the apparently uneven Zn plating can be observed and gradually develop into dendrites after 40 minutes (Video S1). In contrast, flat and compact plating was observed without any dendrites on Zn surface in the hybrid electrolyte (Video S2). Moreover, reversible plating/stripping tests in Zn||Ti batteries were conducted to investigate the CE and Zn chemistry stability. For pure aqueous electrolyte, the low CE (less than 90%) combined with severe parasitic reactions results in failure to reach the cut-off voltage after only a few dozen cycles. The sudden and irreversible rise of the polarization voltage appeared in corresponding voltage profiles (Figure 4c). In a comparison, ultra-stable Zn plating/stripping and high CE (≈99.3%) can be achieved (Figure S25 and S26), because hybrid electrolytes effectively inhibit water activity and modulate the solvated sheath to achieve inhibition of parasitic reactions. In particular, the initial CE is low because the Zn encounters a lattice-fitting phase (or reshaped of the Zn coordination) on the Ti foil as the previous report.[29a] In particular, the relatively increased polarization in Zn symmetric cells and Zn||Ti cells based on hybrid electrolytes can be attributed to reduced ionic conductivity of the electrolytes (Figure S27). According to the above experimental and theoretical studies, the overall mechanism of using sulfolane-H_2O hybrid electrolyte to improve the stability of Zn anode is shown in Figure 4d.

As a proof-of-concept, we chose the frequently-used $V_2O_5{\cdot}nH_2O$ (VOH) as the cathode active material to assemble the Zn||VOH full batteries with different electrolytes (Figure S28). The XRD result and SEM image of VOH are shown in Figure S29. The safety is an important factor in practical applications. When the hybrid electrolyte is 1:1, the safety test shows that it is non-flammable (Video S3). By contrast, the 2:1 electrolyte is flammable (Figure 5a; Video S4). The initial voltage of the pure aqueous electrolyte is about 1.45 V and gradually decreases to 1.28 V after 200 minutes of rest, which may be related to the spontaneous intercalation of Zn^{2+} ions, V species dissolution, and the spontaneous side reaction process between the Zn anode and the electrolyte (Figure 5b). Meanwhile, the initial

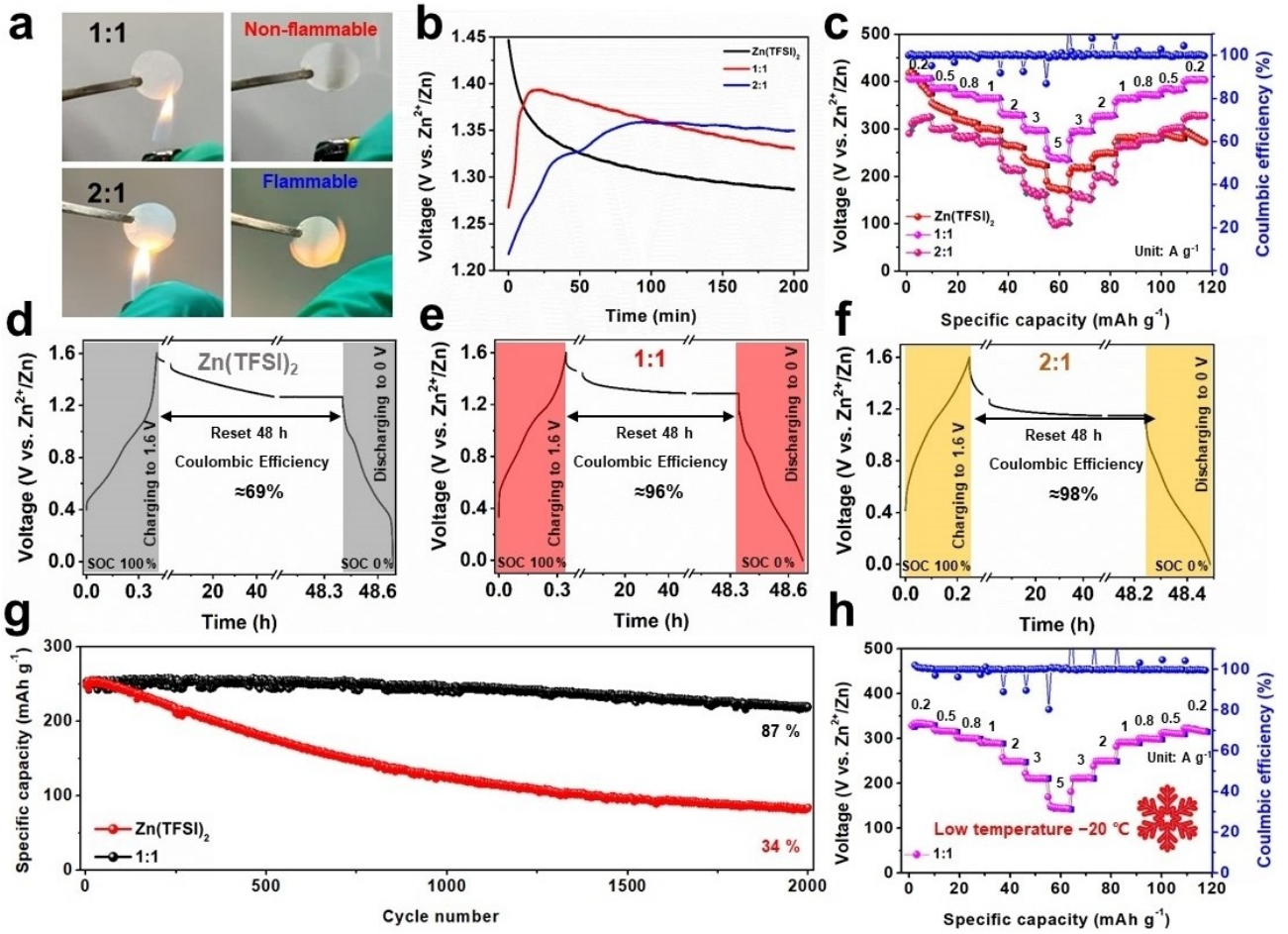

Figure 5. Electrochemical performance of Zn||VOH batteries under different electrolytes. a) Flammability test of 1:1 and 2:1 electrolytes. b) Standing voltage changes and c) rate performances of Zn||VOH batteries with $Zn(TFSI)_2$, 1:1, and 2:1 electrolytes, respectively. d) Self-discharge test of Zn||VOH batteries with different electrolytes. First charged to 1.6 V at 1 $A g^{-1}$ and then full discharged to 0 V after 48 h resting period. g) Long-term cycle performance of Zn||VOH batteries at 5 $A g^{-1}$. h) Rate performances of Zn-VOH batteries based on 1:1 electrolyte at low temperature of −20 °C.

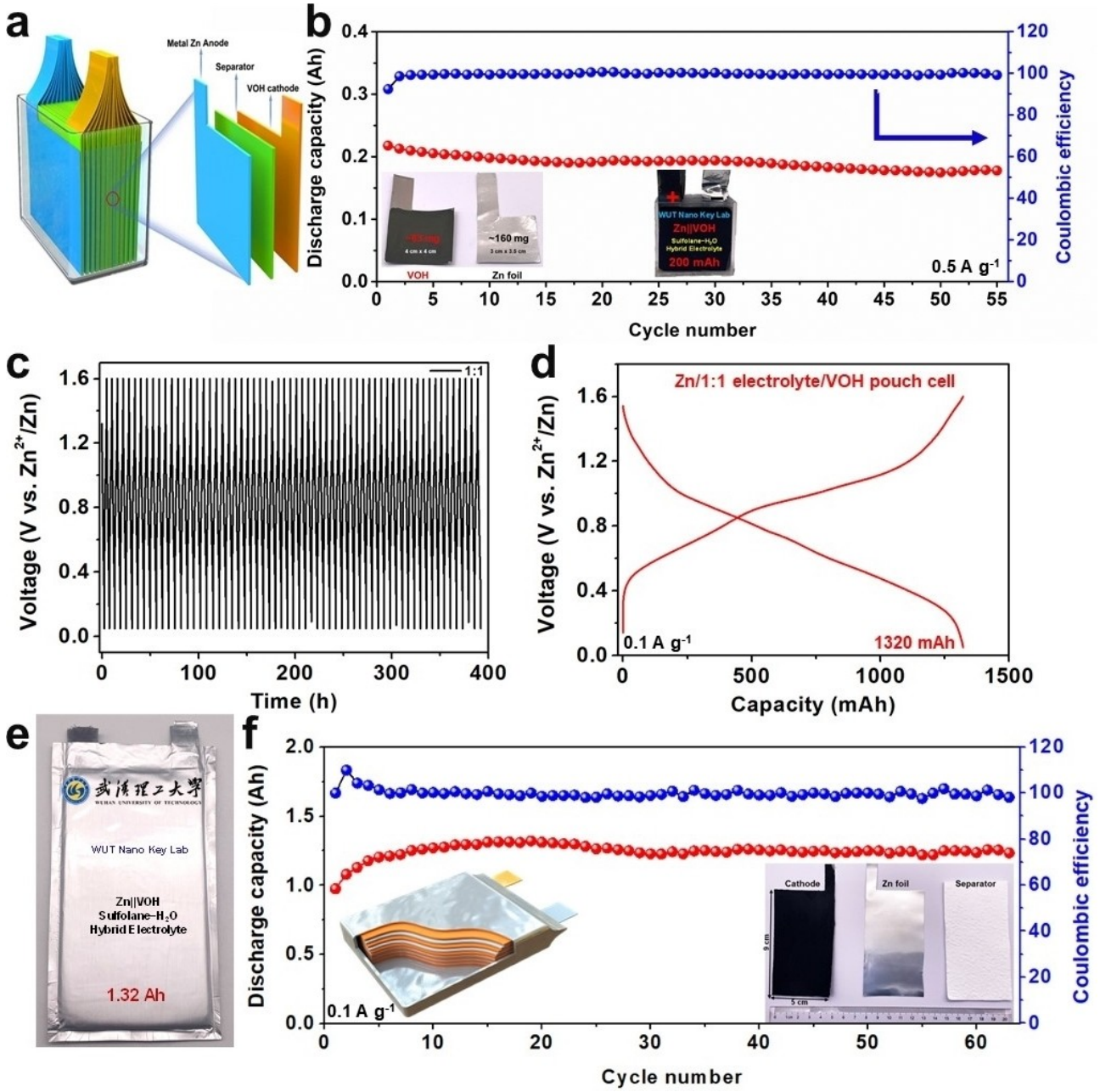

Figure 6. a) Schematic diagram of multi-layer modular Zn||VOH cell and b) corresponding cycle performance; the inserts are electrodes and modular Zn||VOH cell photos. c) The voltage-time curves, d) capacity-time curves, e) optical photo, and cycle performance of high-capacity 1.32 Ah multi-layer Zn||VOH pouch cell; the inserts are schematic diagram, electrodes, and separator of Zn||VOH pouch cell.

voltages of the batteries using hybrid electrolytes were 1.27 and 1.22 V and increased to 1.39 and 1.36 V during the subsequent resting process, respectively. This can be attributed to the decreased permeability of the electrolyte to the material due to its slightly higher viscosity. The electrochemical performances of the battery under different electrolytes were further tested (Figure 5c). For pure aqueous electrolyte and sulfolane-H_2O hybrid electrolytes, the ratio of 1:1 electrolyte exhibits the best electrochemical performance due to the proper introduction of sulfolane. Furthermore, the proven inhibition of both parasitic reactions at Zn anode and V species dissolution at VOH cathode also make for excellent self-discharge inhibition behaviour of the Zn-VOH full battery (Figure S30). The pure aqueous electrolyte shows capacity retention of 69 % after standing for 48 h. As a comparison, 1:1 (96 %) and 2:1 (98 %) electrolytes exhibit much higher capacity retention due to the upgraded water environment in hybrid electrolytes (Figure 5d–f). Therefore, synthetically considering the safety and electrochemical performance, the 1:1 electrolyte was selected as the most suitable electrolyte for the full battery. Benefiting from the excellent stability of the Zn anode, the

Zn-VOH battery used 1:1 hybrid electrolyte exhibits a much longer cycle life (the capacity retention rate of 87% after 2000 cycles) than pure aqueous electrolyte (the capacity retention rate of 34% after 2000 cycles) at 5 $A g^{-1}$ (Figure 5g). Furthermore, 1:1 electrolyte exhibits greater stability and CE than pure aqueous electrolytes, proving effective inhibition of parasitic reactions (Figure S31). Moreover, the excellent low-temperature performance of the full battery has also been demonstrated due to the rupture of the H_2O–H_2O hydrogen bond network (Figure 5h). The full battery used 1:1 electrolyte can work well even at −20 °C and maintain a high specific capacity (83% Vs. room temperature at 0.2 $A g^{-1}$), which is much better than aqueous electrolyte (Figure S32).

Low-capacity coin cells have ideal internal space, sufficient electrolyte, and simple structure that makes it easier to achieve relatively uniform plating under the even strong pressure provided by the external battery cases. The assembly of high-capacity pouch cells at the Ah level, leading to practical applications, is a key step in ZMBs research as the complex multi-layer internal structure places more stringent requirements on the stability of the Zn electrode. To further evaluate the practicability of sulfolane-H_2O hybrid electrolytes (1:1), the multi-layer homemade modular cell and pouch cell were assembled. The multi-layer homemade modular cell (19 cathode + 19 anode) can be easily assembled without encapsulation due to stable electrolytes, showing the huge potential for large-scale replication (Figure 6a). It exhibits the open circuit voltages (OCV) of 1.45 V, higher than coin cell due to the better electrolyte infiltration (Figure S33). Its maximum capacity is 217.8 mAh and 177.8 mAh after running for over 55 cycles with 81.6% capacity retention (Figure 6b). The assembly of a large-capacity cell has rarely been reported so far, and especially the successful realization of homemade modular cell without encapsulation required. The multi-layer pouch cell (6 cathode + 6 anode) with high capacity (over 1.32 Ah) were assembled to demonstrate the practicability of 1:1 hybrid electrolyte. When using the pure aqueous $Zn(TFSI)_2$ electrolyte, the assembled pouch cell appear a short circuit after only 2 cycles (≈13 h) due to the high capacity (1.22 Ah) exacerbating the formation of dendrites during the electroplating process. The disassembled cell separator shows significant Zn dendrite penetration (Figure S34). The stable cycle performance based 1:1 hybrid electrolyte is far better than pure aqueous electrolyte (Figure 6c). It shows the maximum capacity 1.32 Ah at current of 0.1 $A g^{-1}$, which is one of the best performances to date (Figure 6d). In particular, to the best of our knowledge, the corresponding area capacity is 4.89 $mAh cm^{-2}$, which is also the best performance to date.[33] In fact, such a high area capacity increases the energy density while placing more stringent requirements on the Zn anode. Even so, the stable cycle of assembled pouch cell demonstrates significant Zn stability optimization (Figure 6e, 6f and Figure S35). Detailed parameters are shown in Table S2. Compared to the pristine pouch cell, no significant change in battery volume after cycling suggests suppressed water splitting. The modular cell and multi-layer pouch cell we developed show excellent application potential in cluster build-up to realize large-scale energy storage applications and provide a new battery assembly insight in aqueous energy storage system.

Conclusion

In summary, we proposed an efficient strategy for hydrogen bond network reconstruction and multifunctional interfaces optimization by configuring the sulfolane-water hybrid electrolytes. It exhibit a series of excellent characteristics such as substantially reduced freezing point, wide ESW, mild pH, and high stability. MD simulations and XAFS analysis indicate that effective regulation of the solvated structure. Further, the construction of multifunctional sulfolane/Zn interface achieve restricted 2D diffusion, effective active water shielding, as well as guided uniform flux of Zn^{2+} ions. Hence, the suppressing parasitic reactions, HER, and dendrites growth promote highly stable Zn plating/stripping, resulting in an exceptionally long cycle life of over 9600 h in Zn symmetrical battery and CE of ≈99.3% in Zn||Ti batteries. The multi-layer homemade modular cell and 1.32 Ah pouch cell were also assembled, further confirming its prospect for practical application.

Acknowledgements

This work was supported by the National Natural Science Foundation of China (52172233, 51832004, 21905218, 51872218, 52072285), the National Key Research and Development Program of China (2020YFA0715000), the Hubei Provincial Natural Science Foundation of China (2019CFA001, 2019CFB519), the Foshan Xianhu Laboratory of the Advanced Energy Science and Technology Guangdong Laboratory (XHT2020-003), the Hainan Provincial Joint Project of Sanya Yazhou Bay Science and Technology City (520LH055), the Sanya Science and Education Innovation Park of Wuhan University of Technology (2021KF0019), and the Fundamental Research Funds for the Central Universities (WUT: 2020IVA036, 2021CG014).

Conflict of Interest

The authors declare no conflict of interest.

Data Availability Statement

The data that support the findings of this study are available from the corresponding author upon reasonable request.

Keywords: Aqueous Zn Metal Batteries · Deep Eutectic Solvents · H_2O Molecules Regulation · Hydrogen Bond Reconfiguration · Solvation Shell

[1] a) N. Zhang, X. Chen, M. Yu, Z. Niu, F. Cheng, J. Chen, *Chem. Soc. Rev.* **2020**, *49*, 4203; b) F. Wang, O. Borodin, T. Gao, X. Fan, W. Sun, F. Han, A. Faraone, J. A. Dura, K. Xu, C. Wang, *Nat. Mater.* **2018**, *17*, 543; c) C. J. M. Melief, *Nat. Mater.* **2018**, *17*, 482.

[2] a) Q. Yang, Q. Li, Z. Liu, D. Wang, Y. Guo, X. Li, Y. Tang, H. Li, B. Dong, C. Zhi, *Adv. Mater.* **2020**, *32*, 2001854; b) L. Kang, M. Cui, F. Jiang, Y. Gao, H. Luo, J. Liu, W. Liang, C. Zhi, *Adv. Energy Mater.* **2018**, *8*, 1801090; c) M. Li, Q. He, Z. Li, Q. Li, Y. Zhang, J. Meng, X. Liu, S. Li, B. Wu, L. Chen, Z. Liu, W. Luo, C. Han, L. Mai, *Adv. Energy Mater.* **2019**, *9*, 1901469; d) B. Tang, L. Shan, S. Liang, J. Zhou, *Energy Environ. Sci.* **2019**, *12*, 3288.

[3] G. D. Smith, R. Bell, O. Borodin, R. L. Jaffe, *J. Phys. Chem. A* **2001**, *105*, 6506.

[4] M. Li, Z. Li, X. Wang, J. Meng, X. Liu, B. Wu, C. Han, L. Mai, *Energy Environ. Sci.* **2021**, *14*, 3796.

[5] Z. Wang, J. Huang, Z. Guo, X. Dong, Y. Liu, Y. Wang, Y. Xia, *Joule* **2019**, *3*, 1289.

[6] a) A. Naveed, H. Yang, Y. Shao, J. Yang, N. Yanna, J. Liu, S. Shi, L. Zhang, A. Ye, B. He, J. Wang, *Adv. Mater.* **2019**, *31*, 1900668; b) X. Jia, C. Liu, Z. G. Neale, J. Yang, G. Cao, *Chem. Rev.* **2020**, *120*, 7795.

[7] H. Yang, Y. Qiao, Z. Chang, H. Deng, X. Zhu, R. Zhu, Z. Xiong, P. He, H. Zhou, *Adv. Mater.* **2021**, *33*, 2102415.

[8] a) C. Huang, X. Zhao, S. Liu, Y. Hao, Q. Tang, A. Hu, Z. Liu, X. Chen, *Adv. Mater.* **2021**, *33*, 2100445; b) Z. Zhao, J. Zhao, Z. Hu, J. Li, J. Li, Y. Zhang, C. Wang, G. Cui, *Energy Environ. Sci.* **2019**, *12*, 1938; c) H. Lu, X. Zhang, M. Luo, K. Cao, Y. Lu, B. B. Xu, H. Pan, K. Tao, Y. Jiang, *Adv. Funct. Mater.* **2021**, *31*, 2103514; d) X. Xie, S. Liang, J. Gao, S. Guo, J. Guo, C. Wang, G. Xu, X. Wu, G. Chen, J. Zhou, *Energy Environ. Sci.* **2020**, *13*, 503; e) X. Guo, Z. Zhang, J. Li, N. Luo, G.-L. Chai, T. S. Miller, F. Lai, P. Shearing, D. J. L. Brett, D. Han, Z. Weng, G. He, I. P. Parkin, *ACS Energy Lett.* **2021**, *6*, 395.

[9] E. Arunan, G. R. Desiraju, R. A. Klein, J. Sadlej, S. Scheiner, I. Alkorta, D. C. Clary, R. H. Crabtree, J. J. Dannenberg, P. Hobza, H. G. Kjaergaard, A. C. Legon, B. Mennucci, D. J. Nesbitt, *Pure Appl. Chem.* **2011**, *83*, 1637.

[10] M. Huggins, *J. Phys. Chem.* **1936**, *40*, 723.

[11] a) J. S. Filhol, M. Neurock, *Angew. Chem. Int. Ed.* **2006**, *45*, 402; *Angew. Chem.* **2006**, *118*, 416; b) Y. Wang, T. Wang, D. Dong, J. Xie, Y. Guan, Y. Huang, J. Fan, Y.-C. Lu, *Matter* **2022**, *5*, 162.

[12] J. Xie, Z. Liang, Y. C. Lu, *Nat. Mater.* **2020**, *19*, 1006.

[13] P. A. Kollman, L. C. Allen, *Chem. Rev.* **1972**, *72*, 283.

[14] a) J. Xu, X. Ji, J. Zhang, C. Yang, P. Wang, S. Liu, K. Ludwig, F. Chen, P. Kofinas, C. Wang, *Nat. Energy* **2022**, *7*, 186; b) J. Wu, Q. Liang, X. Yu, Q. F. Lü, L. Ma, X. Qin, G. Chen, B. Li, *Adv. Funct. Mater.* **2021**, *31*, 2011102; c) W. Yang, X. Du, J. Zhao, Z. Chen, J. Li, J. Xie, Y. Zhang, Z. Cui, Q. Kong, Z. Zhao, C. Wang, Q. Zhang, G. Cui, *Joule* **2020**, *4*, 1557; d) L. Cao, D. Li, E. Hu, J. Xu, T. Deng, L. Ma, Y. Wang, X. Q. Yang, C. Wang, *J. Am. Chem. Soc.* **2020**, *142*, 21404; e) D. Feng, F. Cao, L. Hou, T. Li, Y. Jiao, P. Wu, *Small* **2021**, *17*, 2103195; f) X. Zhao, X. Zhang, N. Dong, M. Yan, F. Zhang, K. Mochizuki, H. Pan, *Small* **2022**, *18*, 2200742.

[15] L. Geng, X. Wang, K. Han, P. Hu, L. Zhou, Y. Zhao, W. Luo, L. Mai, *ACS Energy Lett.* **2022**, *7*, 247.

[16] S. Cai, X. Chu, C. Liu, H. Lai, H. Chen, Y. Jiang, F. Guo, Z. Xu, C. Wang, C. Gao, *Adv. Mater.* **2021**, *33*, 2007470.

[17] a) X. Lin, G. Zhou, M. J. Robson, J. Yu, S. C. T. Kwok, F. Ciucci, *Adv. Funct. Mater.* **2021**, *31*, 2109322; b) J. Liu, C. Yang, X. Chi, B. Wen, W. Wang, Y. Liu, *Adv. Funct. Mater.* **2022**, *32*, 2106811.

[18] Q. Zhang, K. Xia, Y. Ma, Y. Lu, L. Li, J. Liang, S. Chou, J. Chen, *ACS Energy Lett.* **2021**, *6*, 2704.

[19] M. Śmiechowski, J. Stangret, *J. Mol. Struct.* **2008**, *878*, 104.

[20] a) J. B. Brubach, A. Mermet, A. Filabozzi, A. Gerschel, P. Roy, *J. Chem. Phys.* **2005**, *122*, 184509; b) L. Scatena, M. Brown, G. Richmond, *Science* **2001**, *292*, 908.

[21] P. Gupta, A. C. Dillon, A. S. Bracker, S. M. George, *Surf. Sci.* **1991**, *245*, 360.

[22] B. Liu, C. Wei, Z. Zhu, Y. Fang, Z. Bian, X. Lei, Y. Zhou, C. Tang, Y. Qian, G. Wang, *Angew. Chem. Int. Ed.* **2022**, *61*, e202212780; *Angew. Chem.* **2022**, *134*, e202212780.

[23] Z. Xia, H. Zhang, K. Shen, Y. Qu, Z. Jiang, *Phys. B* **2018**, *542*, 12.

[24] Y. Huang, X. Zhang, Z. Ma, Y. Zhou, W. Zheng, J. Zhou, C. Q. Sun, *Coord. Chem. Rev.* **2015**, *285*, 109.

[25] H. J. Lunk, H. Hartl, M. A. Hartl, M. J. Fait, I. G. Shenderovich, M. Feist, T. A. Frisk, L. L. Daemen, D. Mauder, R. Eckelt, A. A. Gurinov, *Inorg. Chem.* **2010**, *49*, 9400.

[26] a) J. Hao, L. Yuan, C. Ye, D. Chao, K. Davey, Z. Guo, S.-Z. Qiao, *Angew. Chem. Int. Ed.* **2021**, *60*, 7366; *Angew. Chem.* **2021**, *133*, 7442; b) H. E. Gottlieb, V. Kotlyar, A. Nudelman, *J. Org. Chem.* **1997**, *62*, 7512.

[27] a) M. Angell, C.-J. Pan, Y. Rong, C. Yuan, M.-C. Lin, B.-J. Hwang, H. Dai, *Proc. Natl. Acad. Sci. USA* **2017**, *114*, 834; b) P. Jaumaux, X. Yang, B. Zhang, J. Safaei, X. Tang, D. Zhou, C. Wang, G. Wang, *Angew. Chem. Int. Ed.* **2021**, *60*, 19965; *Angew. Chem.* **2021**, *133*, 20118.

[28] a) D. Marx, M. E. Tuckerman, J. Hutter, M. Parrinello, *Nature* **1999**, *397*, 601; b) N. Dubouis, A. Serva, R. Berthin, G. Jeanmairet, B. Porcheron, E. Salager, M. Salanne, A. Grimaud, *Nat. Catal.* **2020**, *3*, 656; c) M. E. Tuckerman, D. Marx, M. Parrinello, *Nature* **2002**, *417*, 925.

[29] a) P. Sun, L. Ma, W. Zhou, M. Qiu, Z. Wang, D. Chao, W. Mai, *Angew. Chem. Int. Ed.* **2021**, *60*, 18247; *Angew. Chem.* **2021**, *133*, 18395; b) Q. Zhang, J. Luan, L. Fu, S. Wu, Y. Tang, X. Ji, H. Wang, *Angew. Chem. Int. Ed.* **2019**, *58*, 15841; *Angew. Chem.* **2019**, *131*, 15988; c) Q. Zhang, J. Luan, Y. Tang, X. Ji, H. Wang, *Angew. Chem. Int. Ed.* **2020**, *59*, 13180; *Angew. Chem.* **2020**, *132*, 13280.

[30] Q. Yang, Y. Guo, B. Yan, C. Wang, Z. Liu, Z. Huang, Y. Wang, Y. Li, H. Li, L. Song, J. Fan, C. Zhi, *Adv. Mater.* **2020**, *32*, 2001755.

[31] A. Bayaguud, X. Luo, Y. Fu, C. Zhu, *ACS Energy Lett.* **2020**, *5*, 3012.

[32] Q. Li, A. Chen, D. Wang, Z. Pei, C. Zhi, *Joule* **2022**, *6*, 273.

[33] a) Q. Zhang, Y. Ma, Y. Lu, X. Zhou, L. Lin, L. Li, Z. Yan, Q. Zhao, K. Zhang, J. Chen, *Angew. Chem. Int. Ed.* **2021**, *60*, 23357; *Angew. Chem.* **2021**, *133*, 23545; b) R. Guo, X. Liu, F. Xia, Y. Jiang, H. Zhang, M. Huang, C. Niu, J. Wu, Y. Zhao, X. Wang, C. Han, L. Mai, *Adv. Mater.* **2022**, *34*, 2202188; c) L. Ma, Q. Li, Y. Ying, F. Ma, S. Chen, Y. Li, H. Huang, C. Zhi, *Adv. Mater.* **2021**, *33*, 2007406.

Manuscript received: October 21, 2022
Accepted manuscript online: December 19, 2022
Version of record online: January 16, 2023